Steam Oxidation and Chromia Evaporation in Ultra-Supercritical Steam Boilers and Turbines

Gordon R. Holcomb

National Energy Technology Laboratory, United States Department of Energy

Albany, Oregon 97321, USA

Abstract

U.S. Department of Energy's goals include power generation from coal at 60% efficiency, which requires steam conditions of up to 760 °C and 340 atm, so-called ultra-supercritical (USC) conditions. Evaporation of protective chromia scales is expected to be a primary corrosion mechanism. A methodology to calculate Cr evaporation rates from chromia scales was developed and combined with Cr diffusion calculations within the alloy (with a constant flux of Cr leaving the alloy from evaporation) to predict Cr concentration profiles and to predict the time until breakaway oxidation. At the highest temperatures and pressures, the time until breakaway oxidation was predicted to be quite short for the turbine blade, and of concern within the steam pipe and the higher temperature portions of the superheater tube. Alloy additions such as Ti may allow for a reduction in evaporation rate with time, mitigating the deleterious effects of chromia evaporation.

Introduction

Goals of the U.S. Department of Energy's Advanced Power Systems Initiatives include power generation from coal at 60% efficiency, which requires steam conditions of up to 760 °C and 340 atm, so-called ultra-supercritical (USC) steam conditions. A limitation to achieving the goal is a lack of cost-effective metallic materials that can perform at these temperatures and pressures. Some of the more important performance limitations are high-temperature creep strength, fire-side corrosion resistance, and steam-side oxidation resistance. Nickel-base superalloys are expected to be the materials best suited for steam boiler and turbine applications above about 675 °C (1). Specific alloys of interest include Haynes 230 and 282, Inconel 617, 625, 718, and 740, Nimonic 105, and Udimet 720Li. Alloy compositions are given in Table I (2-9).

Steam-side oxidation can result in several adverse conditions: general section loss from material thinning, deep localized section loss from internal oxidation (that may also provide crack initiation sites), dimensional changes that are critical in airfoils, and downstream erosion from oxide spallation. Evaporation of protective chromia scales may also be an issue at the higher temperatures and pressures of USC steam turbines. The evaporation of chromia scales in steam is the focus of the research presented here.

In prior work, a methodology to calculate the expected chromia evaporation rate as a function of temperature, pressure, gas velocity, and steam chemistry was developed for chromia forming alloys (10). The methodology was experimentally validated at low pressures and gas velocities by how well its kinetics predictions matched atmospheric pressure oxidation experiments in air plus water vapor environments. At 760 °C and 340 atm, evaporation rates as high as 5.18×10^{-8} kg/m^2/s of $CrO_2(OH)_2(g)$ were predicted for rotating high pressure (HP) turbine blade

components (10). This is equivalent to 0.08 mm per year of solid Cr loss. It was speculated that chromia evaporation upstream of the HP turbine, such as in the superheater, could partially saturate the steam with $CrO_2(OH)_2(g)$ and reduce the chromia evaporation rate.

The research presented here expands upon the prior work by 1) the use of new determinations of the thermodynamic properties of $CrO_2(OH)_2(g)$, 2) expanding the methodology from flat plate components to cylindrical geometries (such as found within superheaters and steam pipes), 3) linking the chromia evaporation in steam to Cr diffusion within the alloy to predict alloy Cr concentration profiles and breakaway oxidation times, and 4) applying the breakaway oxidation predictions to a hypothetical superheater-steam pipe-HP turbine steam path, where the effects of $CrO_2(OH)_2(g)$ saturation along the steam path are applied.

Chromia Evaporation

The oxidation of alloys protected by the formation of Cr_2O_3 (chromia formers) can undergo scale loss due to reactive evaporation of chromium-containing gas species. Water vapor increases the evaporation loss by allowing the formation of $CrO_2(OH)_2(g)$, which for these conditions has a higher vapor pressure than $CrO_3(g)$. $CrO_3(g)$ is the predominate Cr gas specie in dry air or oxygen (11). The formation of $CrO_2(OH)_2(g)$ can be written as:

$$\tfrac{1}{2}Cr_2O_3(s) + H_2O(g) + \tfrac{3}{4}O_2(g) = CrO_2(OH)_2(g) \quad [1]$$

Evaporation can change the overall oxidation kinetics from parabolic behavior to linear kinetics or even to breakaway oxidation. Linear kinetics can arise after scale growth from oxidation, which decreases with increasing scale thickness, matches the scale loss from reactive evaporation (12). The change in scale thickness, x, with time, t, can then be described in terms of the parabolic rate constant, k_p, and the linear reactive evaporation rate, k_e, as:

$$\frac{dx}{dt} = \frac{k_p}{x} - k_e \qquad [2]$$

At long times or high reactive evaporation rates, a limiting scale thickness, x_L, arises that is given by:

$$x_L = \frac{k_p}{k_e} \qquad [3]$$

In this case metal loss rates are linear, but still involve diffusion through a protective scale. Rapid metal loss can occur when reactive evaporation of Cr depletes the scale (and sometimes the substrate metal) of Cr (13-14). Decreased Cr in the scale or metal can lead to the formation of less protective oxides, such as Fe-Cr oxides in Fe-Cr base alloys. Unprotective scales can lead to rapid metal loss, or "break-away" oxidation.

A detailed methodology for calculating evaporation rates in a variety of environments was presented in earlier work for gas flow over a flat plate (10). Two basic equations were developed: Eq. 4 for laminar flow and Eq. 5 for turbulent flow:

$$k_e\left(\frac{kg}{m^2 s}\right) = 0.664\, Re_L^{0.5} Sc^{0.343} \frac{D_{AB} M_{CrO_2(OH)_2}}{LRT} P_{CrO_2(OH)_2} \qquad [4]$$

$$k_e\left(\frac{kg}{m^2 s}\right) = 0.0592\, Re_L^{0.8} Sc^{0.333} \frac{D_{AB} M_{CrO_2(OH)_2}}{LRT} P_{CrO_2(OH)_2} \qquad [5]$$

where Re_L and Sc are the dimensionless Reynolds and Schmidt numbers, D_{AB} is the gaseous diffusion coefficient between $CrO_2(OH)_2$ and the solvent gas (m^2/s), $M_{CrO2(OH)2}$ is the molecular mass of $CrO_2(OH)_2$ (kg/g-mol), L is the length (m) in the flow direction of the flat plate, $P_{CrO2(OH)2}$ is the partial pressure of $CrO_2(OH)_2$ (atm), R is the gas constant (8.20594×10^{-5} m^3atm/K g-mol), and T is the absolute temperature (K). The dimensionless Reynolds and Schmidt numbers are defined as:

$$Re_L = \frac{\rho_s u L}{\eta} \quad [6]$$

$$Sc = \frac{\eta}{\rho_s D_{AB}} \quad [7]$$

where ρ_s is the density of the solvent gas (kg/m^3), η is the absolute viscosity (kg/m/s), and u is the gas velocity (m/s). The Gibbs energy for reaction 1, Opila *et al*. (15), was used to determine $P_{CrO2(OH)2}$. This is a change from the prior work (10), where the thermodynamic data of Gindorf *et al*. (16) was used.

To expand the above methodology for use in pipes and to include possible saturation effects, it is useful to rewrite Eqs. 4-5 in more general terms that include the average Sherwood number (Sh_{Ave}) and to allow for the value of the partial pressure of $CrO_2(OH)_2(g)$ well away from the metal surface, $P^{\circ}_{CrO2(OH)2}$, to slow down the evaporation (Eqs. 4-5 assumed $P^{\circ}_{CrO2(OH)2}$ was zero):

$$k_e\left(\frac{kg}{m^2 s}\right) = Sh_{Ave}\frac{D_{AB}M_{CrO_2(OH)_2}}{LRT}\left(P_{CrO_2(OH)_2} - P^{\circ}_{CrO_2(OH)_2}\right) \quad [8]$$

where Sh_{Ave} is equal to $0.664Re_L^{0.5}Sc^{0.343}$ for laminar flow over flat plates and to $0.0592Re_L^{0.8}Sc^{0.333}$ for turbulent flow over flat plates.

For flow within circular tubes, Eq. 8 is used but with a different expression for Sh_{Ave}. For the analysis that follows, the Dittus-Boelter equation (17-18) was used for Sh_{Ave} for turbulent conditions:

$$Sh_{Ave} = 0.023 Re_d^{0.8} Sc^{0.4} \quad [9]$$

where Re_d is the same as Re_L but with the diameter, d, instead of the plate length, L, in Eq. 6. For rough pipes the use of an expression for Sh_{Ave} that incorporates a friction factor, such as that of Petukov (18-19) can be used.

Chromia Evaporation in Cyclic Oxidation Tests

Cyclic oxidation tests were conducted for up to 2000 hourly cycles in air with 37-38% water vapor. Each hourly cycle consisted of 55 minutes in the furnace, withdrawal from the furnace, holding for 3.4 minutes, and then placement back into the furnace. The samples experienced rapid heating and cooling rates, and were oriented such that the gas flow was parallel to their surfaces. More experimental details can be found in prior work (20).

A goal of the cyclic tests was to evaluate alloys for use in USC boilers and turbines. Scale exfoliation, resulting in part from thermal expansion mismatch between the alloy and the scale, is an important failure mechanism in boiler tubes (21). The use of thermal cycles is an aggressive test of scale exfoliation tendencies. While some alloys did exhibit scale exfoliation in the cyclic tests (20), no scale exfoliation was observed during tests on the alloys discussed below.

Results for two alloys, Haynes 230 and Inconel 740, are shown in Figures 1 and 2 respectively. The Haynes 230 results show the influence of gas velocity—a factor of 4 increase in gas velocity resulted in a factor of 2 increase in evaporation, which is consistent with Eqs. 6 and 8. The dashed lines in Fig. 1 show the evaporation rate from the model, with an activity of chromia of 0.05. This low chromia activity presumably arises from chromia depletion in the outer portion of the oxide scale as chromia is lost to evaporation. The results for two different heats of Inconel 740 in Fig. 2 show two different behaviors. The heat with the □ symbols initially had a similar evaporation rate as the Haynes 230 results. The evaporation rate decreased after about 800 cycles. The other heat, with + symbols, exhibited much less chromia evaporation. Differences between these heats are discussed in the mitigation section.

Chromium Diffusion

After evaporation causes the overall oxidation kinetics to become linear and to have a steady state scale thickness (Eq. 3), the flux of Cr away from the scale via evaporation must equal the flux of Cr to the scale via Cr diffusion within the alloy. If there is insufficient arrival of Cr to the surface, then the chromia scale will not be maintained and breakaway oxidation would be expected to eventually occur.

To model Cr diffusion within the alloy with a constant flux of Cr leaving the surface, the transient heat transfer model of Incropera and DeWitt (18) within a semi-infinite solid and with a constant surface heat flux was used. The underlying mathematics between heat and mass transfer are the same, so this model was used with appropriate mass transfer parameters. The overall equation for the concentration of Cr as a function of x (depth from the surface into the alloy, m) and t (time, s), $C_{Cr}(x,t)$ is:

$$C_{Cr}(x,t) = C_{Cr}^{\circ} - \frac{2k_e}{M_{CrO_2(OH)_2}}\sqrt{\frac{t}{\pi D_{Cr}}}\exp\left(-\frac{x^2}{4D_{Cr}t}\right) + \frac{k_e x}{M_{CrO_2(OH)_2} D_{Cr}}\operatorname{erfc}\left(\frac{x}{2\sqrt{D_{Cr}t}}\right) \quad [10]$$

where C_{Cr}° is the bulk alloy Cr concentration (mol/m^3) (Table I), D_{Cr} is the diffusion coefficient of Cr (m^2/s), and erfc is the complementary error function. For the concentration of Cr at the surface as a function of time, Eq. 10 simplifies to:

$$C_{Cr}(0,t) = C_{Cr}^{\circ} - \frac{2k_e}{M_{CrO_2(OH)_2}}\sqrt{\frac{t}{\pi D_{Cr}}} \quad [11]$$

And the surface concentration is equal to zero at time t^*:

$$t^* = \frac{\pi D_{Cr}}{4}\left(\frac{M_{CrO_2(OH)_2} C_{Cr}^{\circ}}{k_e}\right)^2 \quad [12]$$

Breakaway oxidation is expected to occur prior to t^*, such as when the surface concentration becomes less than some critical value. There is no universally accepted critical surface

concentration, but it cannot be less than zero. So t^* is used as a proxy for the time until breakaway oxidation will occur.

At the temperatures in a steam turbine, the diffusion coefficient, D_{Cr}, is an effective diffusion coefficient and is a combination of lattice, D_{Cr}^{L}, and grain boundary, D_{Cr}^{gb}, diffusion. The relationship used is based on cubic grains of size λ (m) and with grain boundary width δ (m) (22):

$$D_{Cr} \cong D_{Cr}^{L} + \frac{2\delta}{\lambda} D_{Cr}^{gb} \qquad [13]$$

The lattice diffusion coefficients were determined using Dictra diffusion simulation software (23) with the Ni-DATA (24) and MOB2 (25) databases. Figure 3 shows lattice diffusion coefficients of Cr in the face-centered-cubic (FCC) phase for alloys of interest as a function of Cr content at 760 °C. The right-most-point for each alloy is at the alloy Cr content. The lower Cr content values represent the alloy where it is locally depleted in Cr near the surface. Figure 3 shows that for many of the alloys an assumption of a constant value for the diffusion coefficient is a good one.

The use of the FCC phase as the basis of lattice diffusion is a simplification of the rather complex nature of these alloys. All of the alloys in Table I are strengthened by the formation of one or more second phases, the amount of which depend upon heat treatment (2-9). Two of these alloys (Nimonic 105 and Udimet 720Li) have very significant amounts of a second phase (gamma prime). Further phase complications can arise from Cr depletion, where the loss of Cr can itself lead to phase changes. An example of this can be seen in Fig. 4, for Inconel 617 exposed to 2000 hourly cycles at 760 °C in air with 37% H_2O at atmospheric pressure. Figure 4

shows a phase transition zone near the oxide interface, presumably from Cr depletion. Internal oxidation, mainly of aluminum, is also present underneath the oxide scale along grain boundaries. Thus, a more comprehensive phase-based treatment of diffusion coefficients may be warranted. However, for the calculations that follow, the values used for the lattice diffusion coefficients are ones from the FCC phase at the Cr content of the alloy (Fig. 3).

Grain boundary diffusion coefficients are estimated based on the work of Paul *et al.* (26) where lattice and grain boundary diffusion coefficients were determined for Inconel 800 (where a grain boundary width of 0.5 nm was used). The estimate is to use the same ratio of grain boundary diffusion to lattice diffusion that was found for Inconel 800, and to use the same grain boundary width of 0.5 nm. This ratio is given by Eq. 14:

$$\frac{D_{Cr}^{gb}}{D_{Cr}^{L}} \cong \exp\left(\frac{12412}{T} - 1.7203\right) \qquad [14]$$

An example of a comparison between calculated and measured Cr diffusion profiles is given in Fig. 5 for Inconel 740 exposed to 2000 hourly cycles at 760 °C (under the same conditions as in Fig 4.). The predicted $CrO_2(OH)_2$ evaporation rate was 2.13×10^{-9} kg/m^{2}s (10). Figure 5a is a backscattered electron image of a cross-section of the metal-scale interface. It shows a very thin oxide scale and a larger thickness of internal oxidation. The internal oxidation is primarily of aluminum. Figure 5b shows the Cr concentration profile measured using X-ray photoelectron spectroscopy (points) and the results of the model of Eqs. 10 and 14 with λ equal to 30 μm and δ equal to 0.5 nm (line). The model is a close fit to the measured points, with the model showing a bit less Cr depletion at the metal scale interface than the measured points. Note that the use of 2000 hours in Fig. 5b is an approximation that overstates the time at temperature (each hourly cycle had a few minutes at lower temperatures).

Using the same procedures as described above for Inconel 740, it was found that other alloys exposed in the same conditions exhibited even more Cr depletion than Inconel 740 did (and more deviation from Eq. 10). However, Eq. 10 only considers Cr depletion from evaporation. Until the steady state conditions of Eq. 3 are met, the alloy is being oxidized at a faster rate than evaporation would indicate. This initial oxidation is an additional source of Cr depletion (27-28), so measured Cr profiles should show more Cr depletion than is found simply by using Eq. 10. Inconel 740 has a smaller k_p than the other alloys of interest (20), so it lost less Cr to scale formation (and thus less deviation from Eq. 10 than the other alloys).

Hypothetical Superheater-Steam Pipe-HP Turbine Steam Path

The combination of gas evaporation of $CrO_2(OH)_2$, gas saturation of $CrO_2(OH)_2$, and Cr depletion in the alloy is illustrated in Fig. 6. Figure 6 represents one section of superheater (SH) tubing or steam pipe of cell length L. The bulk partial pressure of $CrO_2(OH)_2$ coming into the cell is $P^{\circ}_{CrO2(OH)2}$ (Incoming). Evaporation within the cell at rate k_e raises the $P^{\circ}_{CrO2(OH)2}$ (Outgoing) by the amount released by evaporation and is shown in Eq. 15.

$$P^{\circ}_{CrO_2(OH)_2\,\text{(Outgoing)}} = P^{\circ}_{CrO_2(OH)_2\,\text{(Incoming)}} + \frac{4k_e LRT}{duM_{CrO_2(OH)_2}} \qquad [15]$$

The effects of saturating the gas phase with $CrO_2(OH)_2$ can then be calculated along the length of a SH tube or steam pipe by combining many cells together. A hypothetical arrangement of a 100 m long, 0.05 m I.D., SH that leads into a 50m long, 0.3 m I.D., steam pipe that leads to a high pressure (HP) turbine is illustrated in Fig. 7. The temperature profile and steam velocities are shown on the left-hand axis, while the evaporation rate is shown on the right-hand axis. The SH and steam pipe each consisted of 160 cells of the type shown in Fig. 6. Saturation results in a 80% reduction in the evaporation rate at the HP turbine.

The steam chemistry used in Fig. 7 and in subsequent calculations was based off of feedwater treatments that are typical of once-through supercritical power plants, i.e., a pH of 8.0-8.5 controlled with ammonia additions (29). At high temperatures, water undergoes dissociation to O_2 and H_2 to levels well above 1 ppb. To estimate the dissolved oxygen required for Eq. 1 at temperature and pressure, the program FactSage 5.5 (30) was used to first determine the amount of NH_3 required for a pH of 8.25 at 25°C: 34.5 ppb. This agreed well with the reported (29) 20-65 ppb NH_3 used for pH control to 8.0 to 8.5. Next FactSage 5.5 was used to find the value of the fugacities of H_2O and O_2 for each temperature and pressure combination from water with 34.5 ppb NH_3. The use of fugacities instead of partial pressures made only a minor difference because the fugacity adjustments tended to cancel each other out.

The time for the alloy Cr level to reach zero at the scale-metal interface, using Eq. 12, is shown in Fig. 8 for the same conditions as in Fig. 7 (and using saturated values for k_e). Haynes 230 was the alloy used. At these conditions, the chromia evaporation at the HP turbine blade is expected to be so great as to deplete the alloy surface of Cr in a few days. The steam pipe inlet is the area of next concern with the time to zero Cr at the alloy surface being predicted to be about 1 year.

The very high temperatures and total pressures of Figs. 7-8 match that of the U. S. Department of Energy's goals of 760 °C and 340 atm. The impact of evaporation at lower temperatures and pressures can be seen in Figs. 9-10, where similar procedures are used to estimate the time it takes for the surface concentration of Cr in the alloy to reach zero. In all cases the SH inlet temperature was taken to be 600 °C. Below 600 °C, ferritic alloys, which would not be expected to form chromia scales, would typically be used.

Figure 9 shows why chromia evaporation is not considered to be of much concern in existing steam boilers and turbines. Modern advanced steam cycles are currently no higher than 630 °C, so the time to breakaway oxidation (for which the time for C(0,t) to reach 0 is being used as an estimate) is well beyond the life span of the boiler or turbine. Another factor limiting chromia evaporation in modern advance steam cycles is that ferritic steels are extensively used, and they do not form chromia scales. So the activity of Cr is lower in the scales, which from Eq. 1 lowers the partial pressure of $CrO_2(OH)_2(g)$, which in turn decreases chromia evaporation (Eq. 8).

Mitigation

Mitigation of these predicted high evaporation rates can be speculated upon. One way would be the use of a non-chromia forming coating. An example would be a thermal barrier coating (TBC), such as one based on yttria stabilized zirconia (YSZ). Such coatings are being postulated for use to reduce turbine blade erosion. This would eliminate the transport path for chromia evaporation. Even if the coating were porous, it would effectively increase the gaseous diffusion boundary layer to the thickness of the coating, thus eliminating much of the detrimental gas velocity effects.

Another mitigation would be to reduce the activity of chromia in the oxide scale, at least at the oxide-gas interface. The Haynes 230 results (Fig. 1) shows that this is already occurring since a chromia activity of 0.05 matches the observed evaporation rate. This is similar to efforts to reduce the activity of chromia in solid oxide fuel cell (SOFC) interconnect development. For example, enough Mn additions to result in outer scales of Mn-Cr spinels instead of chromia is expected to reduce the evaporation of Cr by a factor of 55 at 700 °C and by a factor of 35 at 800 °C (31). This is equivalent to a chromia activity of 0.0006 at 760 °C. However, other properties

of the alloy would have to be maintained—Mn alloy additions generally reduce the high-temperature creep strength of steels (32), so Mn additions are not expected to be used in these applications. However, additions of Ti, which can lead to the formation of TiO_2 at the outer oxide surface (33), may be more useful for these alloys since Ti is already being used in some of the candidate alloys. Table II lists the results for Haynes 230, Inconel 740, and Inconel 617. The results for Inconel 617 were obtained in cyclic oxidation tests similar to those used for Hayes 230 and Inconel 740. Table II shows that variations in Mn from 0.1 to 0.5 have little effect on the apparent chromia activity. It also shows that Ti levels in the 1.6-1.8 range may be enough to significantly reduce chromia evaporation.

Note that the evaporation model assumes a constant chromia evaporation rate. However, the actual situation appears to be more complex with the activity of chromia and chromia evaporation decreasing with time as chromia is removed from the oxide. It may also be the case that higher evaporation rates may lead to more rapid decreases in chromia evaporation, so even modest amounts of Ti, and perhaps Mn, may be enough to reduce chromia evaporation to manageable rates.

Conclusions

A methodology that was developed to calculate Cr evaporation rates from Cr_2O_3 with a flat planar geometry (10), was expanded upon to allow for interior cylindrical geometries, and to allow for the effects of $CrO_2(OH)_2$ saturation within the gas phase. This approach was combined with Cr diffusion calculations within the alloy (with a constant flux of Cr leaving the alloy from evaporation) to predict Cr concentration profiles as a function of exposure time and to predict the time until the alloy surface concentration of Cr reaches zero. This time is a rough prediction of

the time until breakaway oxidation.

A hypothetical super heater (SH) tube, steam pipe, and high pressure (HP) turbine steam path was assembled and examined with the methodology. At the U. S. Department of Energy's goals of 760 °C and 340 atm, the time until breakaway oxidation was predicted to be quite short for the turbine blade, and of concern within the steam pipe and the higher temperature portions of the SH tube. The predicted time until breakaway oxidation increases dramatically with decreases in temperature and total pressure.

Possible mitigation techniques were discussed, including lowering the activity of chromia in the oxide scale by adding Ti to the alloy, and thermal barrier coating (TBC) use on HP turbine blades for both erosion and chromia evaporation protection.

References

1. R. Viswanathan, J. F. Henry, J. Tanzosh, G. Stanko, J. Shingledecker, B. Vitalis, and R. Purgert, *Journal of Materials Engineering and Performance*, **14**, 281 (2005).

2. Haynes 230 Alloy, H-3135C, Haynes International, Kokomo, IN (2008).

3. Haynes 282 Alloy, H-3172A, Haynes International, Kokomo, IN (2008).

4. Inconel Alloy 617, SMC-029, Special Metals Corporation, Huntington, WV (2005).

5. Inconel Alloy 625, SMC-063, Special Metals Corporation, Huntington, WV (2006).

6. Inconel Alloy 718, SMC-045, Special Metals Corporation, Huntington, WV (2007).

7. Inconel Alloy 740, SMC-090, Special Metals Corporation, Huntington, WV (2004).

8. Nimonic Alloy 90, SMC-081, Special Metals Corporation, Huntington, WV (2007).

9. Udimet Alloy 720, SMC-106, Special Metals Corporation, Huntington, WV (2004).

10. G. R. Holcomb, *Oxidation of Metals*, **69**, 163 (2008).

11. H. C. Graham and H. H. Davis, *J. Am. Ceram. Soc*., 54, 89 (1971).

12. C. S. Tedman, Jr., *J. Electrochem. Soc*. **113**, 766 (1966).

13. H. Asteman, J.-E. Svensson, L.-G. Johansson, and M. Norell, *Oxidation of Metals*, **52**, 95 (1999).

14. H. Asteman, J.-E. Svensson, M. Norell, and L.-G. Johansson, *Oxidation of Metals*, **54**, 11 (2000).

15. E. J. Opila, D. L. Myers, N. S. Jacobson, I. M. B. Nielsen, D. F. Johnson, J. K. Olminsky, and M. D. Allendorf, *Journal of Physical Chemistry A*, **111**, 1971 (2007).

16. C. Gindorf, K. Hilpert, and L. Singheiser, in *Solid Oxide Fuel Cells (SOFC VII)*, H. Yokokawa and S. C. Singhal, Editors, PV 2001-16, p. 793, The Electrochemical Society Proceedings Series, Pennington, NJ (2001).

17. R.H.S. Winterton, *International Journal of Heat and Mass Transfer*, **41**, 809 (1998).

18. F. P. Incropera and D. P. DeWitt, *Fundamentals of Heat and Mass Transfer*, 5th Ed., pp. 268-70, 491-492, 508, John Wiley & Sons, New York (2001).

19. B. S. Petukhov, in *Advances in Heat Transfer*, Vol 6, T. F. Irvine and J. P. Hartnett, Editors, p. 503, Academic Press, New York (1970).

20. G. R. Holcomb, D. E. Alman, Ő. N. Doğan, J. C. Rawers, K. K. Schrems, and M. Ziomek-Moroz, in *Proceedings of the 21st Annual Conference on Fossil Energy Materials*, Knoxville, TN, April 30-May 1, 2007, U.S. Department of Energy, Office of Fossil Energy, Advanced Research Materials (2007).

21. A. I. G. Wright and P. F. Tortorelli, "Program on Technology Innovation: Oxide Growth and Exfoliation on Alloys Exposed to Steam," EPRI, Palo Alto, CA: 2007. 1013666.

22. X. Peng, J. Yan, Y. Zhou and F. Wang, *Acta Materialia*, **53**, 5079 (2005).

23. Dictra, Diffusion Simulation Software, Version 24, Thermo-Calc Software AB, Stockholm, Sweden (2006).

24. N. Saunders, *Ni-DATA*, Version 7, Thermotech Ltd, Surrey Technology Centre, Surrey, UK (2000).

25. MOB2, Mobility Database, Version 2.0, Royal Institute of Technology, Foundation of Computational Thermodynamics, Stockholm, Sweden (1999).

26. A. R. Paul, K. N. G. Kaimal, M. C. Naik and S. R. Dharwadkar, *Journal of Nuclear Materials*, **217**, 75 (1994).

27. D. P. Whittle, D. J. Evans, D. B. Scully and G. C. Wood, *Acta Met.* **15**, 1421 (1967).

28. D. P. Whittle, G. C. Wood, D. J. Evans and D. B. Scully, *Acta Met.*, **15**, 1747 (1967).

29. *Steam*, 40th ed., S. C. Stultz and J. B. Kitto, Editors, pp. 3.8-3.9, 42.11, Babcock & Wilcox, Barberton, Ohio (1992).

30. C. W. Bale, A. D. Pelton, W. T. Thompson, G. Eriksson, K. Hack, P. Chartrand, S. Decterov, J. Melançon, and S. Petersen, FactSage 5.5, Thermfact and GTT-Technologies (2007).

31. G. R. Holcomb and D. E. Alman, *Scripta Materialia*, **54**, 1821 (2006).

32. F. Masuyama, *ISIJ International*, **41**, 612 (2001).

33. F. S. Pettit and G. H. Meier, "Fundamental Studies of the Durability of Materials for Interconnects in Solid Oxide Fuel Cells," Final Report, DOE Award: DE FC26 02NT41578, September 30, 2006.

Table I. Alloy Composition (wt%) and Bulk Alloy Cr Concentration (C_{Cr}°) for alloys of interest (2-9).*

Alloy	Fe	Cr	Ni	Co	Mo	Ti	Al	B ppm	Mn	Other	C_{Cr}° mol/m^3
Haynes 230	1.5	22	Bal	2.5	2		0.3	75	0.5	0.02 La 14 W 0.4 Si 0.1 C	0.0380
Haynes 282	0.75	19.5	Bal	10	8.5	2.1	1.5	50		0.15 Cu 0.075 Si 0.06 C	0.0310
Inconel 617	1.5	22	Bal	12.5	9	0.3	1.15	30	0.5	0.25 Cu 0.5 Si 0.1 C	0.0354
Inconel 625	2.5	21.5	Bal	0.5	9	0.2	0.2		0.25	3.65 Nb 0.25 Si 0.05 C	0.0349
Inconel 718	Bal	19	52	0.5	3.05	0.9	0.5	30	0.175	5.125 Nb 0.15 Cu 0.175 Si 0.04 C	0.0299
Inconel 740	0.7	25	Bal	20	0.5	1.8	0.9		0.3	2 Nb 0.5 Si 0.03 C	0.0387
Nimonic 105	0.5	14.85	Bal	20	5	1.2	4.7	65	0.5	0.075 Zr 0.1 Cu 0.5 Si 0.085 C	0.0229
Udimet 720Li		16	Bal	14.75	3	5	2.5	150		1.25 W 0.038 Zr 0.015 C	0.0249

*Source values that were ranges are listed as the midpoint of the range. Source values that were maximums are listed as half the maximum. Only Nb is listed for sources that gave a value or range for Nb+Ta. Source values for Pb, P, and S are omitted.

Table II. Apparent chromia activity.

Alloy	Mn	Ti	Apparent Chromia Activity
Haynes 230	0.5	--	0.05
Inconel 617	0.1	0.3	0.05
Inconel 740 (Fig. 2 □ heat)	0.3	1.6	Initially 0.05 Then ~0.0006
Inconel 740 (Fig. 2 + heat)	0.3	1.8	~0.0006

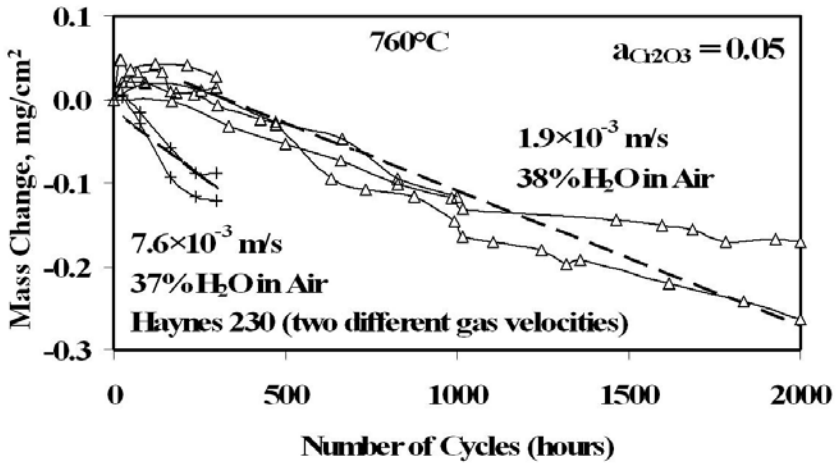

Figure 1. Mass change measurements for Haynes 230 exposed at 760 °C in moist air at two different gas velocities. The dotted lines are the predicted mass change due to chromia evaporation with a chromia activity of 0.05.

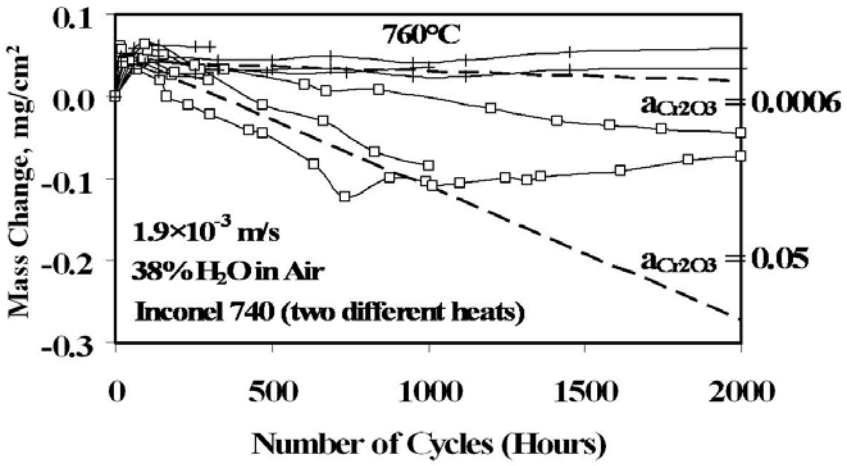

Figure 2. Mass change measurements for two different heats of Inconel 740 exposed at 760 °C in moist air. The dotted lines are the predicted mass changes due to chromia evaporation with chromia activities of 0.05 and 0.0006.

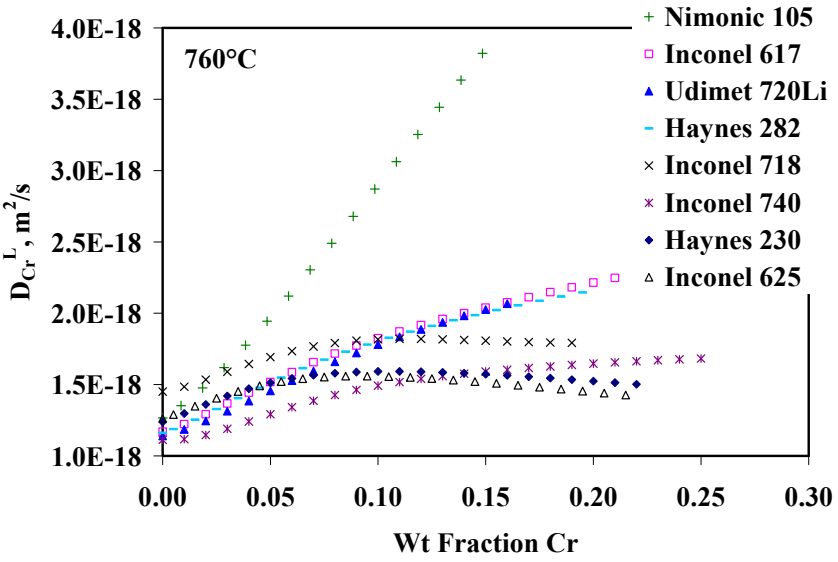

Figure 3. Lattice diffusion coefficients at 760 °C for Cr in the FCC phase of nickel base superalloys determined using Dictra diffusion simulation software (23) with the Ni-DATA (24) and MOB2 (25) databases.

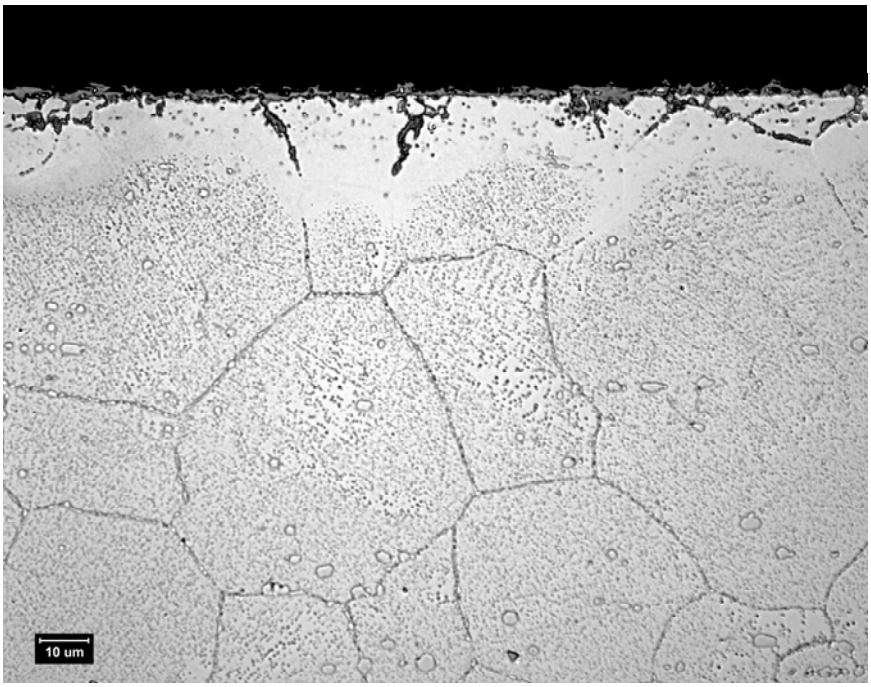

Figure 4. Results of cyclic oxidation of Inconel 617 at 760 °C in air plus 37% H_2O after 2000 hourly cycles. This is a bright field image after etching (50% concentrated nitric acid, 50% glacial acetic acid).

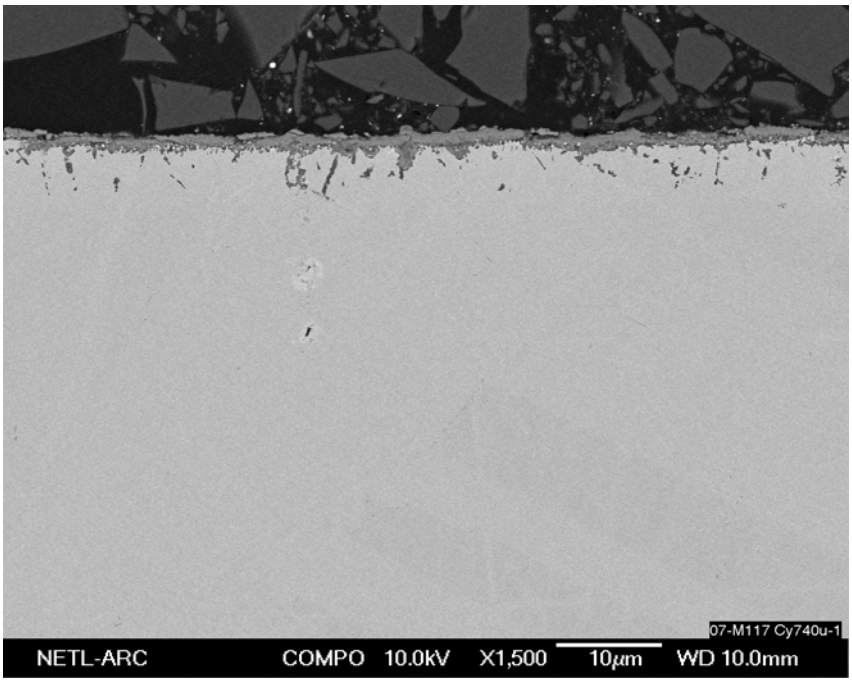

A

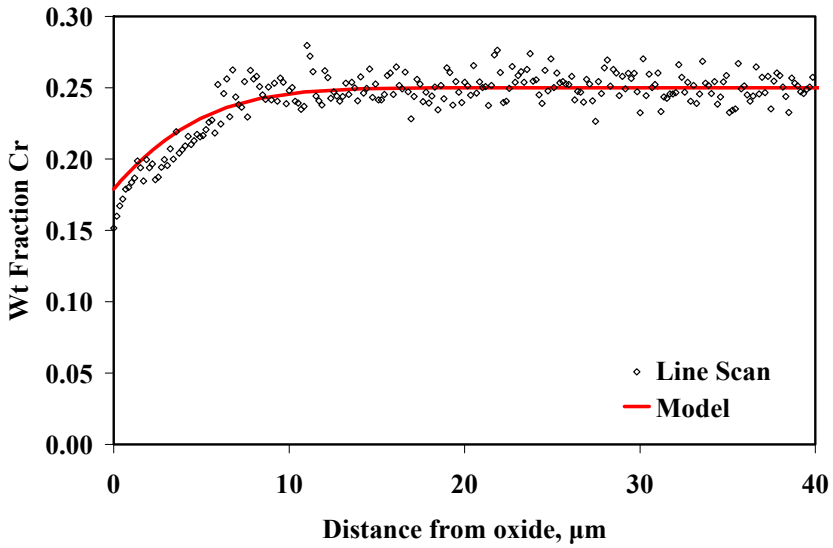

B

Figure 5. Results of cyclic oxidation of Inconel 740 at 760 °C in air plus 37% H_2O after 2000 hourly cycles: a) is a backscattered electron image of the cross-section, b) is the Cr profile from experiment (points) and Eq. 10 (line).

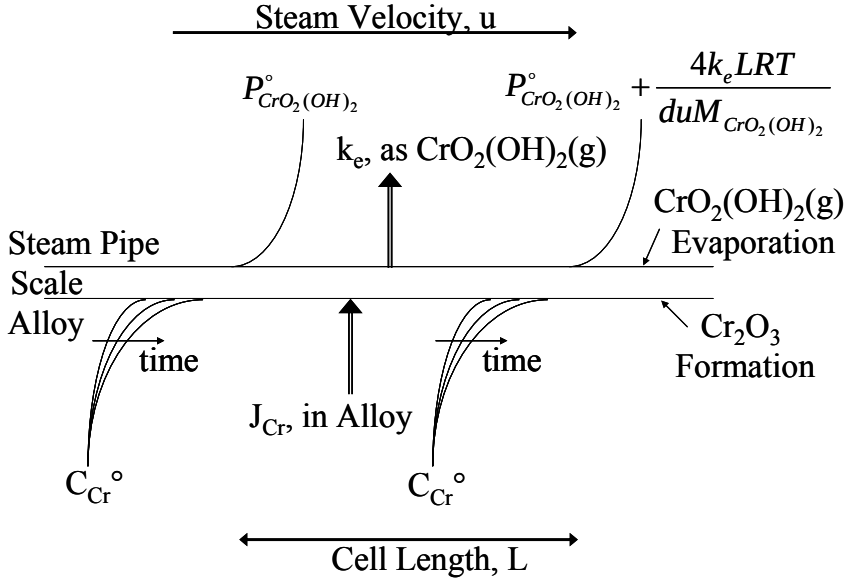

Figure 6. The combination of gas evaporation of $CrO_2(OH)_2$, gas saturation of $CrO_2(OH)_2$, and Cr depletion in the alloy is illustrated. This represents one section of superheater tubing or steam pipe of cell length L.

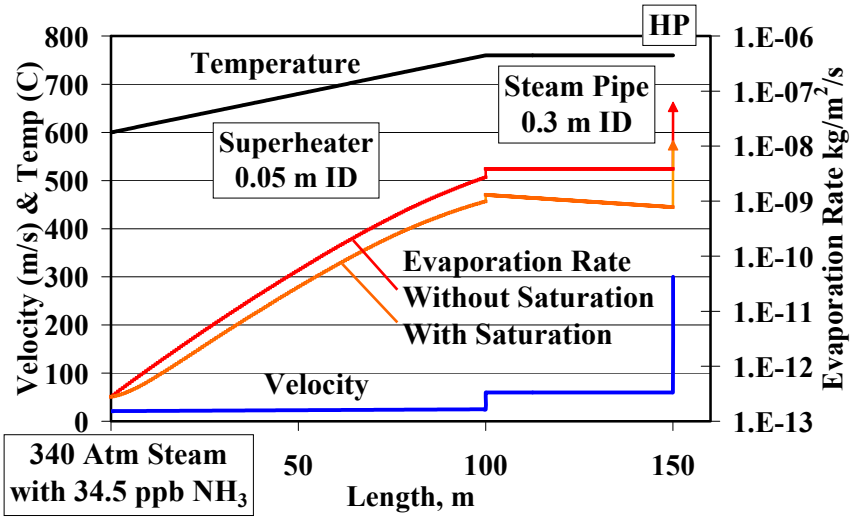

Figure 7. The effects of gas saturation is shown for a hypothetical arrangement of a 100m long SH that leads into a 50m steam pipe that leads to a high pressure (HP) turbine. Saturation results in a 80% reduction in the evaporation rate at the HP turbine.

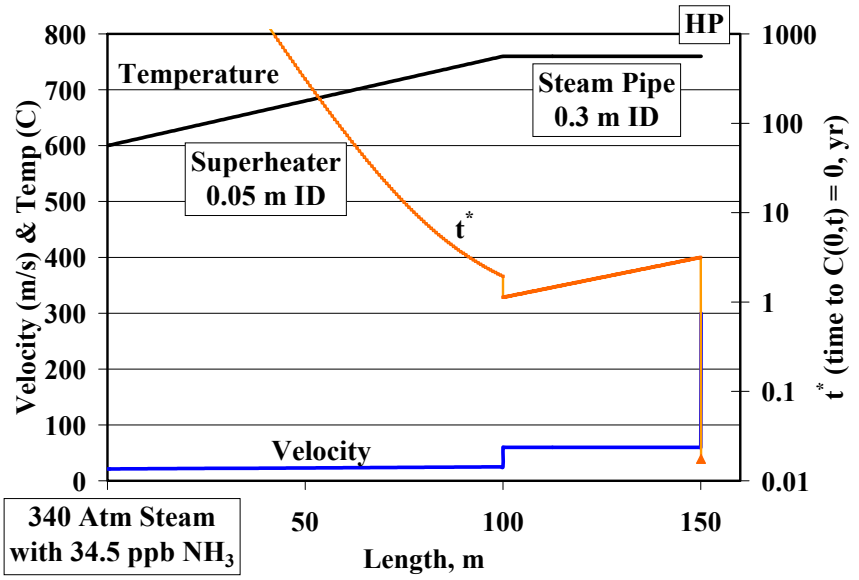

Figure 8. The predicted time for the Cr level at the scale-metal interface to reach zero. Haynes 230 was the alloy system used in this estimate.

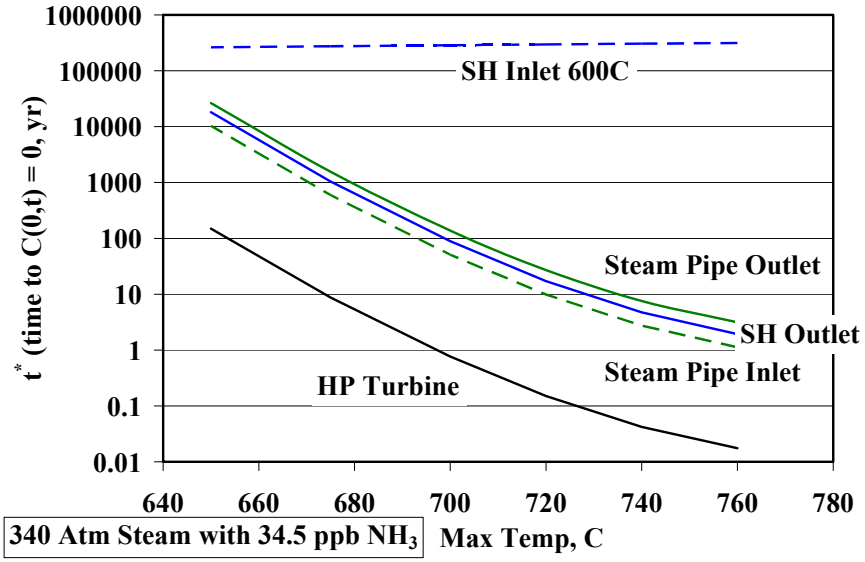

Figure 9. The effects of temperature on the estimate of the time it takes for the surface concentration of Cr in the alloy to reach zero, at 340 atm. Haynes 230 was the alloy system used in this estimate.

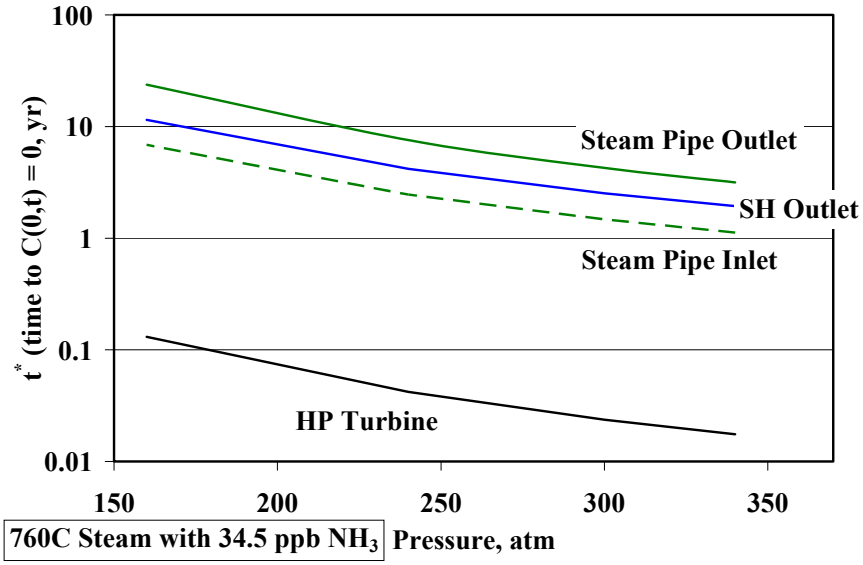

Figure 10. The effects of pressure on the estimate of the time it takes for the surface concentration of Cr in the alloy to reach zero, at 760 °C. Haynes 230 was the alloy system used in this estimate.

Figure Captions

Figure 1. Mass change measurements for Haynes 230 exposed at 760 °C in moist air at two different gas velocities. The dotted lines are the predicted mass change due to chromia evaporation with a chromia activity of 0.05.

Figure 2. Mass change measurements for two different heats of Inconel 740 exposed at 760 °C in moist air. The dotted lines are the predicted mass changes due to chromia evaporation with chromia activities of 0.05 and 0.0006.

Figure 3. Lattice diffusion coefficients at 760 °C for Cr in the FCC phase of nickel base superalloys determined using Dictra diffusion simulation software (23) with the Ni-DATA (24) and MOB2 (25) databases.

Figure 4. Results of cyclic oxidation of Inconel 617 at 760 °C in air plus 37% H_2O after 2000 hourly cycles. This is a bright field image after etching (50% concentrated nitric acid, 50% glacial acetic acid).

Figure 5. Results of cyclic oxidation of Inconel 740 at 760 °C in air plus 37% H_2O after 2000 hourly cycles: a) is a backscattered electron image of the cross-section, b) is the Cr profile from experiment (points) and Eq. 10 (line).

Figure 6. The combination of gas evaporation of $CrO_2(OH)_2$, gas saturation of $CrO_2(OH)_2$, and Cr depletion in the alloy is illustrated. This represents one section of superheater tubing or steam pipe of cell length L.

Figure 7. The effects of gas saturation is shown for a hypothetical arrangement of a 100m long SH that leads into a 50m steam pipe that leads to a high pressure (HP) turbine. Saturation results in a 80% reduction in the evaporation rate at the HP turbine.

Figure 8. The predicted time for the Cr level at the scale-metal interface to reach zero. Haynes 230 was the alloy system used in this estimate.

Figure 9. The effects of temperature on the estimate of the time it takes for the surface concentration of Cr in the alloy to reach zero, at 340 atm. Haynes 230 was the alloy system used in this estimate.

Figure 10. The effects of pressure on the estimate of the time it takes for the surface concentration of Cr in the alloy to reach zero, at 760 °C. Haynes 230 was the alloy system used in this estimate.